Optical and structural properties of metalorganic-vapor-phase-epitaxy-grown InAs quantum wells and quantum dots in InP

R. Leonelli, C. A. Tran, J. L. Brebner, J. T. Graham, and R. Tabti

Département de Physique et Groupe de Recherche en Physique et Technologie des Couches Minces, Université de Montréal, Case Postale 6128, Succ. "A," Montréal, Québec, Canada H3C 3J7

R. A. Masut

Département de Génie Physique et Groupe de Recherche en Physique et Technologie des Couches Minces, École Polytechnique, Case Postale 6079, Succ. "A," Montréal, Québec, Canada H3C 3A7

S. Charbonneau

Institut des Sciences des Microstructures, Conseil National de Recherches du Canada, Ottawa, Ontario, Canada K1A 0R6

InAs single strained quantum wells and nanoclusters have been synthesized by low-pressure metalorganic-vapor-phase epitaxy. The samples were obtained by depositing InAs layers on InP with coverages ranging from several monolayers to a fraction of a monolayer and subsequently overgrowing with InP. These heterostructures were characterized by high-resolution x-ray diffractometry, steady-state and time-resolved photoluminescence, and photoluminescence excitation spectroscopy. In the case of the InAs quantum wells, the experimental x-ray diffraction patterns are in agreement with patterns simulated within the framework of dynamical diffraction theory, assuming that the InAs/InP interfaces are sharp and that the InAs unit cell is tetragonally distorted. The photoluminescence of the quantum wells reveals a series of discrete peaks whose energy positions can be well reproduced by a finite square-well model with a valence-band offset ΔE_{hh} of 240 meV. The excitation spectrum of a one-monolayer-thick quantum well exhibits two resonances which are attributed to heavy- and light-hole excitonic transitions. The fractional InAs monolayers were deposited on terraced InP surfaces. Their x-ray diffraction spectra indicate that the InAs nucleates into nanoclusters. A shift toward higher energies of their optical emission is observed and is attributed to a quantum effect caused by lateral confinement of the excitonic wave function. Time-resolved photoluminescence and photoluminescence excitation spectra show that there is enough overlap of the excitonic wave function between adjacent nanoclusters to result in the formation of delocalized excitonic states. The InAs nanoclusters thus form a quantum dot superlattice.

I. INTRODUCTION

There has been continuing interest in ultrathin InAs-based quantum well structures because of their particular structural and electronic properties[1-8] as well as their significant potential for optoelectronic devices.[9,10] Of special interest is the capacity to control the growth process sufficiently well to be able to grow less than one monolayer (ML) of InAs on a terraced substrate. By analogy with the GaAs/Al$_x$Ga$_{1-x}$As system, where a preferential lateral growth from the step edges of the substrate surface occurs,[11-13] it is expected that the deposited InAs forms nanoclusters.[14,15] The actual fabrication of such a system is, however, strongly dependent on the fundamental growth modes of the epitaxial technique used. In particular, one has to consider the possible diffusion of the deposited InAs in the host material. In the case of the InAs/GaAs system, it is still not clear whether the observed properties of fractional monolayer films should be interpreted in terms of alloy formation, exciton quantum confinement, or exciton localization.[2,14,16]

InAs/InP ultrathin heterostructures could be easier to grow because of a smaller lattice mismatch between the two compounds and also because of the possibility of reduced interdiffusion associated with the interchange of the group V rather than the group III element. In this paper, we report on the structural and optical properties of thin InAs single strained quantum wells (SSQW's) and nanoclusters grown by low-pressure metalorganic-vapor-phase epitaxy (MOVPE) on (001) oriented and vicinal (001) InP substrates tilted 2° towards [100]. A comparative study of high-resolution x-ray diffractometry (HRXRD), low temperature steady-state photoluminescence (PL), time-resolved photoluminescence (TRPL), and photoluminescence excitation spectroscopy (PLE) indicates that (i) under the growth conditions used, the deposited InAs films grow coherently and are fully strained with no significant As diffusion in the InP host matrix, (ii) the emission characteristics of the InAs SSQW's grown on oriented substrates are consistent with the predictions of a finite square-well model, (iii) the InAs nanoclusters grown on terraced InP substrates form quantum dots which laterally confine the

excitons, and (iv) the extent of the excitonic wave function in the InP matrix is sufficient to give rise to coupling between the dots which results in the presence of delocalized excitonic states.

The paper is organized as follows. The sample preparation and the experimental conditions are described in Sec. II. In Sec. III, the optical and structural properties of InAs SSQW's are presented while Sec. IV is devoted to those of InAs nanoclusters. The experimental results are discussed in Sec. V. Finally, we summarize the results and draw conclusions in Sec. VI.

II. SAMPLES AND EXPERIMENTS

The samples were prepared by MOVPE in a horizontal cold-wall quartz reactor. The growth procedure involved the deposition of an InP buffer layer, followed by a single deposition of InAs and terminated by the deposition of an InP cap layer. The growth apparatus is equipped with a fast-switching run-vent gas manifold at the reactor inlet and all the valves are computer controlled. Details of this system have been reported elsewhere.[17] The Fe doped InP substrates were either (001) oriented or misoriented by $2°\pm0.5°$ from (001) towards [100] (hereafter called 2°-off substrates). Tertiarybutylarsine (TBAs), trimethylindium (TMI), and pure phosphine were used as source materials. The carrier gas was Pd-purified H_2 and the total flow rate in the reactor was maintained at 50 standard $cm^3 s^{-1}$. All of the samples were grown under a reactor pressure of 40 Torr and at a substrate temperature of 600 °C. The TBAs and TMI flow rates were set at 0.81 and 9.17×10^{-2} $\mu mol\,s^{-1}$, respectively. This corresponds to a nominal As/In ratio of 8.8. The P/In ratio chosen was 300, in order to adjust the phosphine flow rate close to the value that produces high-quality homoepitaxial InP layers. Under these conditions, the growth rate is 3 ± 0.3 Å s^{-1} for InAs and 2.4 ± 0.1 Å s^{-1} for InP. The InP/InAs interface is obtained by simultaneously turning to vent the TMI and phosphine flows. After a purge of 3 s, the TMI and TBAs are reintroduced simultaneously. InAs/InP interfaces are obtained by turning to vent the TMI and TBAs flows, purging

the reactor for 3 s, and then reintroducing the TMI and phosphine. More details of this growth procedure have been reported in Refs. 8 and 18. A description of the samples studied in this work is given in Table I.

HRXRD was carried out using a Philips diffractometer equipped with a four-crystal Ge monochromator operated in the (220) reflection mode. The Cu $K\alpha_1$ beam $(\lambda_{\text{Cu }K\alpha_1} = 1.540\,56$ Å) was incident on the sample through a slit of 1×1 mm^2 cross section at the end of the monochromator.

For the optical measurements, the samples were mounted strain-free in a helium flow cryostat. The PL was excited using the 514-nm line of an argon-ion laser. The signal was dispersed by a 1-m spectrometer (0.5 meV resolution) and detected by a liquid-nitrogen-cooled Ge p-i-n photodiode using conventional lock-in techniques. The PL spectra were taken with excitation densities of 200 mW cm^{-2}. The PLE spectra were obtained using a Ti:sapphire tunable laser pumped by an argon-ion laser. For the PLE measurements, the excitation density was kept at 10 W cm^{-2}.

The TRPL experiments were performed using a cavity-dumped rhodamine dye laser synchronously pumped by a mode-locked argon-ion laser. The resulting 5 ps pulses were at a wavelength of 595 nm and the repetition rate was 4 MHz. In order to avoid any nonlinear response of the samples, the peak excitation density was maintained at 10 kW cm^{-2} (approximately 1.5×10^{11} photons cm^{-2}). The TRPL signal was dispersed by a 0.25-m double spectrometer (1 meV resolution) and detected with a cooled In-Ga-As photomultiplier using the time-correlated photon counting technique. The nominal time resolution of the system is 450 ps. Time-resolved spectra were obtained by acquiring a series of decay curves at 2 meV intervals over the spectral range of interest. Each curve was deconvolved from the system time response with a Fourier transform method. The actual time resolution was thus improved to better than 100 ps. The time-resolved spectra were then reconstructed.

III. InAs SSQW'S

Figure 1 shows the experimental symmetrical (004) and asymmetrical (224) diffraction patterns of sample

TABLE I. Structural parameters and PL energies E_{PL} of the InAs/InP single heterostructures investigated in this work. For all samples, the InAs layer was sandwiched between InP buffer and cap layers with nominal thicknesses of 600 and 120 nm, respectively.

Sample	Nominal coverage δ_N (ML)	Substrate orientation	E_{PL} (eV)	Attributed coverage δ_A (ML)
S1	4.0	(001)	1.11	4
S2	3.0	(001)	1.09	>4
			1.15	>3
			1.289	2
S3	2.0	(001)	1.18	3
			1.287	2
S4	1.0	(001)	1.346	1
S5	1.0	2° off	1.33	>1
S6	0.8	2° off	1.354	
S7	0.3	2° off	1.388	
S8	0.2	2° off	1.392	
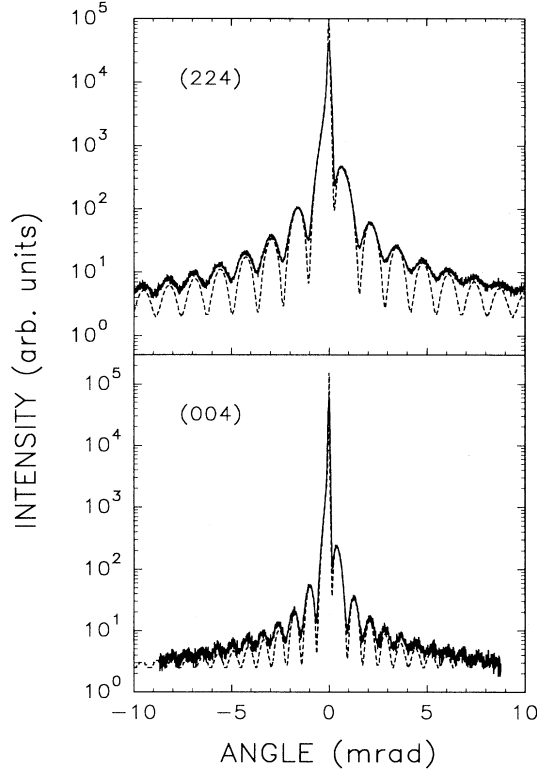
FIG. 1. (004) and (224) HRXRD diffraction patterns of a 1 ML InAs SSQW capped with a 116 nm InP layer. Solid lines: experimental data; dashed lines: simulated pattern using the dynamical theory discussed in the text.

S4, which consists of an InAs layer with nominal coverage $\delta_N = 1$ ML (the strained InAs monolayer thickness is 3.1 Å) grown on a (001) oriented InP substrate and buffer layer and covered with an InP cap layer. The wave diffracted from the InP cap layer is decoupled and phase shifted with respect to the wave scattered from the InP substrate. The interference between the two waves can be observed in the diffraction pattern as an intensified Pendellösung effect.[19]

The main peak in the center of every pattern is the InP Bragg peak. The satellite peaks extending to right and left are the interference fringes of the InP cap layer. The angular fringe peak spacing ω is related to the InP cap layer thickness t according to

$$\omega = \frac{\lambda \mid \gamma_h \mid}{t \sin(\theta_B)}, \tag{1}$$

where λ is the x-ray wavelength, θ_B is the kinematic Bragg angle, and γ_h is the direction cosine of the diffracted beam with respect to the inward normal to the surface.[19] However, the relative position between the main InP Bragg peak and the Pendellösung fringes is a direct measure of the phase shift between the diffracted waves originating from the two decoupled InP layers. This phase shift depends on the product of the strain and the thickness of the InAs sandwiched layer, and is sensitive to a monolayer thickness variation of the InAs layer

if full coverage is assumed.[3,20] Moreover, the symmetric reflections are sensitive to the lattice strain perpendicular to the crystal surface only, while the asymmetric ones are sensitive to the perpendicular as well as to the parallel lattice strain.

Simulated diffraction curves were obtained for both cases using a computer program developed by Fewster at Philips, based on the solution of the Tagaki-Taupin equations of the dynamical diffraction theory.[21] Our model assumed a perfectly abrupt interface between InP and InAs and a zero value for the in-plane mismatch (coherent epitaxy). According to elasticity theory, the lattice strains parallel and perpendicular to the interface in the InAs layer are then given by

$$\epsilon_{xx} = \epsilon_{yy} = \frac{a_{InP} - a_{InAs}}{a_{InAs}} = -0.0312, \tag{2a}$$

$$\epsilon_{zz} = -\frac{2c_{12}}{c_{11}} \left(\frac{a_{InP} - a_{InAs}}{a_{InAs}} \right) = 0.0340, \tag{2b}$$

where c_{11} and c_{12} are the elastic moduli of InAs. The simulated diffraction patterns, also shown in Fig. 1, are in excellent agreement with the experimental ones. This is indicative of the high structural quality of the InAs/InP heterostructure and demonstrates that the InAs unit cell is tetragonally distorted. Simulations obtained under the same assumptions for all the other SSQW samples were also in good agreement with the experimental data, indicating that the average thickness of the layers is close to the nominal thickness δ_N. X-ray diffraction patterns are also remarkably sensitive to variations in composition. We have simulated the HRXRD corresponding to the structure of sample S4 with a single monolayer of $InAs_x P_{1-x}$ instead of InAs. A displacement of the simulated structure on the shoulder of the InP main peak with respect to the experimental one was clearly observed for $x \leq 0.9$.

Figure 2 shows the steady-state PL from samples S1–S4 [1 to 4 ML coverage on (001) oriented substrates]. The spectra consist of discrete peaks whose full width at half maximum (FWHM) varies from 20 to 35 meV. These peaks can be unambiguously associated with monolayer islands of different thicknesses and their energy positions, given in Table I, are in good agreement with many previous reports.[4,5,7] As will be discussed in Sec. V, these PL spectra together with the HRXRD patterns of Fig. 1 show that there is negligible As diffusion in the InP buffer or cap layers.

The number of PL peaks observed in a given sample depends on the topography of the InP buffer layer just before InAs deposition. Because of preferential lateral growth,[13] it is expected that InAs deposited on a partially covered InP buffer will first fill any voids present, thus leading to more pronounced variations in the thickness of the InAs layers than if the InP buffer were nearly fully covered when the InAs growth was initiated. The lateral extent of the resulting islands also plays a major role in the intensity, energy, and FWHM of the PL peaks. The higher intensity of the lower-energy PL peaks in a given sample is expected since, because of efficient exciton transfer towards lower-lying energy states, extended
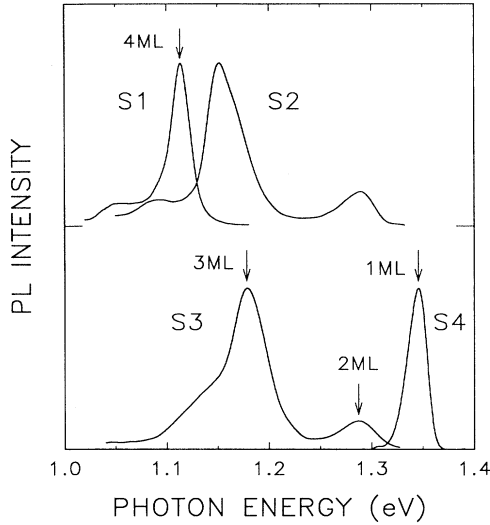
FIG. 2. Steady-state PL spectra obtained at 8 K from samples S1 ($\delta_N = 4$ ML), S2 ($\delta_N = 3$ ML), S3 ($\delta_N = 2$ ML), and S4 ($\delta_N = 1$ ML). The excitation power density was kept at 200 mW cm^{-2}. The arrows indicate the energy positions chosen for the square-well model calculation shown in Fig. 8.

islands of thicknesses higher than average will open major radiative recombination channels even if they occupy a relatively small area.[22] The presence of islands having sizes of the same order as the exciton diameter or of impurities will result in exciton localization which is usually evidenced by a redshift of the order of the half-width at half maximum of the PL peaks.[22–24] The presence of islands with sizes much smaller than the exciton diameter will generate exciton scattering and result in some broadening of the PL peaks both on their low- and high-energy sides.[25] In what follows, we assumed that the actual energy of a SSQW transition could be estimated within 20 meV by the associated peak of highest energy. These peaks are marked with arrows in Fig. 2.

IV. InAs NANOCLUSTERS

We have also deposited InAs submonolayers on vicinal (001) InP substrates tilted 2° towards [100]. The substrate surface ideally consists of two adjacent staircase terraces of one monolayer height with steps running along the [110] and [1$\bar{1}$0] directions as shown in Fig. 3. The terraces are about 60 Å on the side. In the initial stages of growth of InAs on InP, InAs is expected to nucleate and advance from each step on the InP buffer layer surface. If the InAs growth is halted before it can cover the whole terrace area and the InP is then overgrown, an array of InAs nanoclusters embedded in the InP matrix is obtained. The lateral dimension of the InAs nanoclusters ranges from 25 Å for 0.2 ML coverage to 50 Å for 0.8 ML coverage.

Figure 4 shows the (004) HRXRD patterns observed from sample S7 ($\delta_N = 0.3$ ML) together with a simulation obtained assuming a coherent 1 ML InAs coverage.
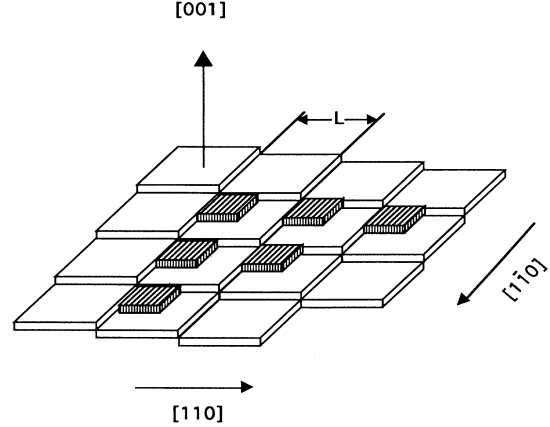
FIG. 3. Vicinal (001) InP surface tilted 2° towards [100]. It consists of two adjacent staircases with steps running along [110] and [1$\bar{1}$0] directions. Shaded boxes represent InAs clusters grown at the terrace step edges.

The simulation of the interference fringes produced by submonolayer coverages constitutes a difficult problem which has not been solved to our knowledge. Nevertheless, the spectra of Fig. 4 show that the deposited InAs does not form an InAs$_{0.3}$P$_{0.7}$ alloy because in such a case, the fringe pattern would be significantly displaced with respect to the main Bragg peak. Thus, under our growth conditions, the deposition of less than one monolayer of InAs on terraced substrates results in the formation of nanoclusters.

Low temperature steady-state PL spectra of samples S4–S8 are shown in Fig. 5. One of the characteristics of all of these samples is that their radiative efficiency is very high: in all samples, the integrated emission from the InAs film is much higher than that from the InP matrix. This indicates that the excitons photogenerated in
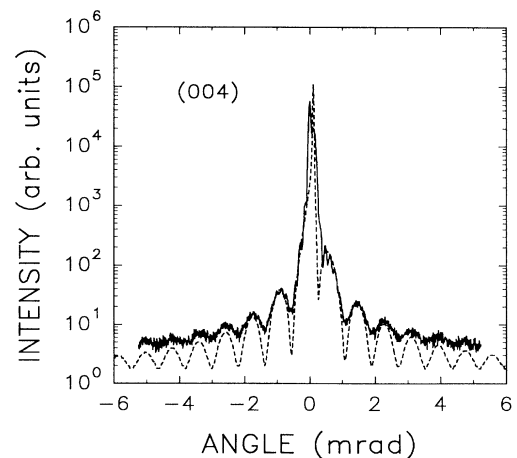
FIG. 4. (004) HRXRD diffraction pattern from sample S7 (0.3 ML, 2° off substrate). Solid line: experimental data; dashed line: simulated pattern using the dynamical theory discussed in the text assuming a 1 ML coverage.
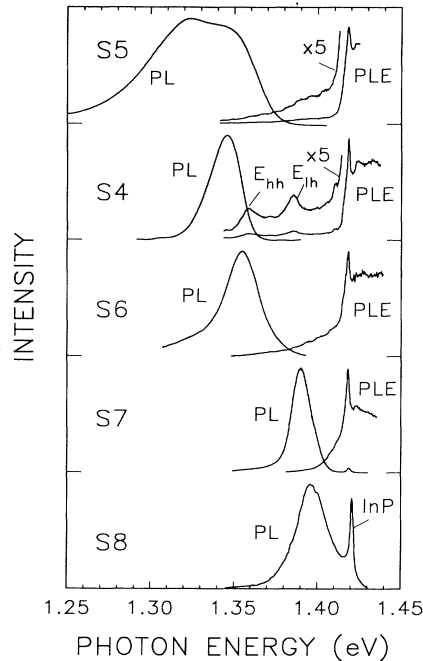
FIG. 5. Steady-state PL and PLE spectra taken at 8 K from samples S5 (1 ML), S4 (1 ML), S6 (0.8 ML), S7 (0.3 ML), and S8 (0.2 ML). Sample S4 was grown on a (001) oriented substrate while samples S5–S8 were grown on 2° off substrates.

FIG. 6. TRPL spectra obtained from samples S4 [1 ML, (001) oriented substrate] and S7 (0.3 ML, 2° off substrate) at 8 K. The peak power density was maintained at 10 kW cm^{-2}. The numbers to the left indicate the delay after excitation in ps.

InP are efficiently captured by the InAs wells or nanoclusters.

A clear shift towards higher energy of the PL from the samples with decreasing submonolayer coverage can be observed. This result can be contrasted to that obtained from similar InAs/GaAs clusters, where no PL shift as a function of coverage was found.[3] The emission FWHM is in the range 14–25 meV for sample S4 [1 ML, (001) substrate] and samples S6–S8 (submonolayer coverage), while it is around 70 meV for sample S5 (1 ML on a 2° off substrate). FWHM's of 70 meV and more were observed in all samples with $\delta_N \geq 1$ ML grown on 2° off substrates. We attribute this increased FWHM to short-range thickness fluctuations at the terrace step edges.

The PLE spectra of samples S4–S7 are also shown in Fig. 5. That of sample S4 exhibits two resonances, attributed to heavy-hole and light-hole transitions. These resonances are not seen in the spectrum of sample S5 [Fig. 5(b)]. However, the rapid reduction in intensity and the final level of the PLE signal for photon energies below the InP band gap are similar to that observed in sample S4. The PLE spectra of samples S6 and S7 ($\delta_N = 0.8$ and 0.3 ML) are markedly different from that of sample S4. There are no resonances and a pronounced tail is observed for photon energies lower than the InP band gap.

Further information on the exciton dynamics in these structures can be obtained from time-resolved PL. Figure 6 shows TRPL spectra from samples S4 [1 ML, (001) substrate] and S7 (0.3 ML, 2° off substrate). During their

rise time, no significant changes in shape or position of the two emission bands can be detected. For times longer than 1 ns, both bands decay with approximately the same lifetime of around 1 ns and spectral diffusion of –3.8 and –2.0 meV ns^{-1} for samples S4 and S7, respectively, can be observed. Figure 7 gives the time evolution during the first nanosecond after excitation of the luminescence, at the position of the peak emissions from samples S4 and S7
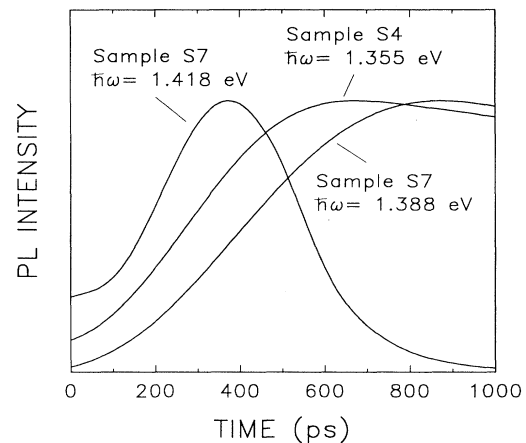
FIG. 7. Time evolution at 8 K of the PL at the peak position of the emissions from samples S4 [1 ML, (001) oriented substrate], S7 (0.3 ML, 2° off substrate), and at the InP emission from sample S7. The peak power density was maintained at 10 kW cm^{-2}. The curves have been deconvolved from the time response of the system.

(dashed lines in Fig. 6) and at the InP band gap energy. As can be seen, the InAs emission is delayed in both samples with respect to that of InP. Furthermore, the InAs emission rise time observed in sample S7 is longer than that of sample 4 by about 200 ps.

V. DISCUSSION

A. InAs SSQW's

As previously stated, any interpretation of the experimental data depends crucially on the assumption that the InP/InAs interfaces are sharp and thus that there is negligible As diffusion in the InP matrix. Unfortunately, even though the dynamical diffraction theory has been used by many authors to quantitatively characterize ultrathin heterostructures, the HRXRD results presented in Sec. III show only that, in the case of SSQW's (samples S1–S4), the total amount of deposited InAs is close to the nominal value δ_N. This is because the phase shift produced by the InAs layer is a function of the product of layer thickness and strain.[19] Since the strain varies linearly with composition, a thicker $InAs_xP_{1-x}$ layer would essentially produce the same diffraction pattern as a thinner InAs layer, assuming both have the same total InAs content.

However, the PL spectra of Fig. 2 show a series of peaks which can be interpreted only in terms of extended flat islands whose thicknesses vary by an integer number of monolayers. Most of the InAs/InP SSQW's reported so far were grown using conventional MOVPE. However, the samples reported by Kobayashi and Kobayashi[7] were grown by the surface photoabsorption method at 350 °C, a temperature too low for any As diffusion or exchange with P atoms. The PL emission from these samples is also in close agreement with that of the SSQW's investigated here.

The PL energy positions were compared to those predicted by a standard finite square-well model, as follows. The effects of strain on the difference between the energies of the conduction and valence bands of InAs were first obtained from the usual expressions:[26]

$$\Delta E_{lh} = \left[2a \left(\frac{c_{11} - c_{12}}{c_{11}} \right) + b \left(\frac{c_{11} + 2c_{12}}{c_{11}} \right) \right] \epsilon_{xx}, \quad (3a)$$

$$\Delta E_{hh} = \left[2a \left(\frac{c_{11} - c_{12}}{c_{11}} \right) - b \left(\frac{c_{11} + 2c_{12}}{c_{11}} \right) \right] \epsilon_{xx}, \quad (3b)$$

where a and b are the deformation potentials and ϵ_{xx} is given by Eq. (2a). The square-well model was then applied with the parameters listed in Table II, leaving the valence-band offset as a free parameter. The PL energies indicated by arrows in Fig. 2 together with the results of the calculation are shown in Fig. 8. The best value for the valence-band offset was found to be $\Delta E_{hh} = 240$ meV ($\Delta E_{hh}/\Delta E_c = 0.25/0.75$), in agreement with the value obtained by Schneider and Wessels.[5] The confinement energies are of the order of the InAs band gap and thus band nonparabolicities should in principle be included in the calculations. However, the result of our calculation is

TABLE II. InAs and InP parameters used in the square-well model calculation. The values were taken from Ref. 27.

	InP	InAs
E_g (eV)	1.42	0.42
m_e^*	0.079	0.024
m_{hh}^*	0.65[a]	0.41
m_{lh}^*	0.12	0.025
lattice constant (Å)	5.8696	6.0588
c_{11} (10^{11} dyn cm^{-2})		8.33
c_{12} (10^{11} dyn cm^{-2})		4.53
a (eV)		-6.0
b (eV)		-1.8

[a]The heavy-hole effective mass in InP is still not very well known. We have preferred to use the value given in Ref. 28 rather than the often cited one of 0.85 which comes from a theoretical calculation (Ref. 29).

insensitive within experimental uncertainties to the effective masses of electrons and holes in InAs because most of their wave functions lie in the InP matrix. This justifies our use of a finite square-well model rather than more sophisticated ones.

The main discrepancy is found for the 1 ML SSQW, whose PL is at a position 30 meV lower than that predicted. This is hardly surprising since in this case the electronic boundary conditions required for any type of calculation are ill defined.[14,16] However, to first order, the energy difference between the heavy- and light-hole transitions should be correctly given by our model. The calculation gives $E_{lh} - E_{hh} = 28$ meV, while the energy difference between the two resonances observed in the PLE spectrum of sample S4 [Fig. 5] is 27 ± 1 meV. This result confirms the assignment of the two resonances to heavy- and light-hole excitonic transitions. To our knowledge, this is the first unambiguous report of a light-hole resonance in a one monolayer quantum well.
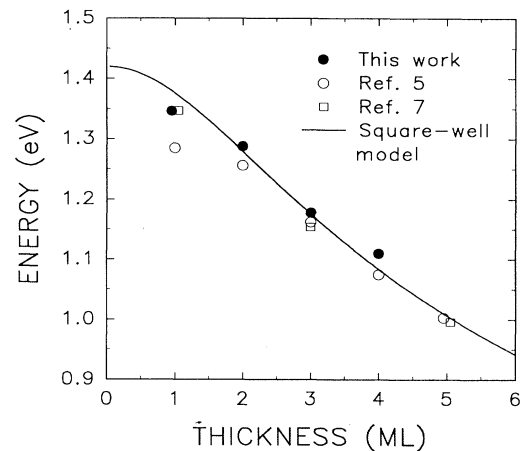
FIG. 8. Dependence of the PL emission energy on well thickness for InAs SSQW's. Also plotted is the calculated dependence using a square-well model with a valence-band offset of 240 meV.

B. InAs nanoclusters

Quantum dots (QD's) are structures which confine electrons and holes in such a small volume that their energy spectrum is discretized in all three spatial directions. This three-dimensional (3D) confinement further increases the energy difference between electron and hole states as compared to the 1D (quantum well) or 2D (quantum wire) cases. As a consequence, the optical transitions originating from QD's are expected to be displaced towards higher energies (blueshift) as the QD volume is reduced.

Several alternative strategies have been used to control the dimensions of semiconductors in the nanometer regime with the aim of realizing QD's.[30,31] The approach used here, based on the preferential nucleation of adatoms near step edges, can in principle produce a unique system of closely packed QD's. The same approach was previously followed by Brandt *et al.*[14] for the InAs/GaAs system. The fact that these authors did not observe any lateral confinement effects such as a blueshift of the PL energies with decreasing coverage led them to conclude that the InAs nanocluster sheet localized the excitons, which otherwise kept their GaAs bulk Bohr radius.

We have shown in the preceding section that, under our growth conditions, there is no significant As diffusion. Furthermore, HRXRD data (Fig. 4) indicate that InAs does nucleate into islands when deposited on a terraced substrate. Therefore the blueshift observed in the PL spectra of the submonolayer samples when δ_N is reduced (Fig. 5) cannot be caused by alloy formation. This blueshift could possibly result from exciton localization at the InAs sheet without quantum confinement effects. It could indeed be argued that if the excitons maintained their InP bulk Bohr radius (approximately 100 Å), their wave function would extend over several terraces. Their emission energies could thus be the same as if they were localized at a one-monolayer-thick $InAs_xP_{1-x}$ QW, with $x = \delta_N$. However, the exciton energy should then be insensitive to the monolayer thickness fluctuations which occur at the terrace boundaries for coverages of one monolayer and more and there should be no abrupt change in the emission FWHM between samples S5 and S6 ($\delta_N = 1$ and 0.8 ML, respectively). We thus conclude that the blueshift of the PL energies with decreasing coverage is a quantum effect caused by a certain degree of lateral confinement of the excitons in the InAs nanoclusters. These nanoclusters therefore form quantum dots.

Further evidence of quantum confinement can be obtained from the PLE spectra of the submonolayer samples shown in Fig. 5. Here again, if the exciton maintained a large Bohr radius, there should be no qualitative difference in the shape of the PLE spectra of samples S5 and S6. The low-energy tail which is observed in the PLE signal of samples S6 and S7, but not of sample S5, indicates that there exists in the former samples a continuous distribution of states which lie below the InP band gap. We associate these states with fluctuations in the InAs nanocluster sizes. Since the PLE signal depends on the absorption coefficient times some transfer coefficient from the excited state to the radiative state, the PLE intensity does not necessarily reflect the density of these higher-energy states. It indicates rather that the excitonic wave function extends further beyond the borders of the InAs QD's if their size is smaller and thus that these excitons can relax more easily to the radiative state observed with PLE.

The time-resolved measurements also reveal differences between one monolayer and submonolayer samples in the relaxation dynamics of excitons. Under our experimental conditions, electron-hole pairs are photogenerated in InP with a large excess energy. These pairs rapidly form excitonlike polaritons[32] which have to relax to the bottleneck of their dispersion curve before they can be converted with significant probability into photons at the surface of the sample.[33] The delay of nearly 400 ps between the excitation pulse and the maximum of the InP emission seen in Fig. 7 can be explained by the time required by the "hot" excitonlike polaritons to relax through optical and acoustic phonon emission. In high-quality bulk InP, the free exciton emission decay time is more than 1 ns. The much faster decay time observed in our samples gives another indication of the high capture rate of the InP free excitons by the InAs films.

In QW's, however, free excitons form 2D polaritons which do not couple to photonlike polaritons propagating perpendicular to the QW planes unless their wave vector is within a homogeneous bandwidth Δ near $|\mathbf{k}| = 0$.[32] The emission rise time thus depends on the rate at which the initially created excitons can relax towards the bottom of their dispersion curve through interactions with phonons. We tentatively explain the longer rise time observed in sample S7 with respect to sample S4 by a reduced interaction of the excitons with acoustic phonons caused by the discretization of the density of states in QD's.[35] As for the decay time, it is strongly influenced by both large- and small-scale fluctuations of the exciton confining potential.[22,24,34,36] If the fluctuations extend over a range of the order of the exciton Bohr radius, exciton localization occurs which results in the spectral diffusion we observe.[22]

The above discussion indicates that there is some coupling between the QD's. This coupling could arise from an overlap of the excitonic wave function of adjacent QD's and result in the formation of delocalized and hence free excitonic states. It could also arise because of phonon-assisted excitonic hopping from one QD to another. It is possible to discriminate between these two cases by a study of the integrated emission lifetime as a function of temperature. Free excitons are characterized by a wave vector $\mathbf{k}$ and, as explained above, momentum conservation requires that only those excitons with a near zero wave vector can recombine radiatively. The fraction n of free excitons near $|\mathbf{k}| = 0$ varies as[37]

$$n(T) \propto (1 - e^{-\Delta/kT}) \qquad (4)$$

and the radiative lifetime of free excitons τ_{Xr} is given by

$$\tau_{Xr}(T) = \frac{\tau_{Xr}^o}{n(T)}. \qquad (5)$$

R. LEONELLI *et al.*
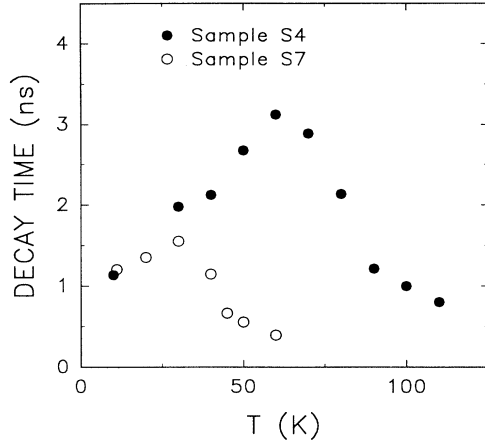
FIG. 9. Average emission decay time τ as a function of temperature for samples S4 [1 ML, (001) oriented subtrate] and S7 (0.3 ML, 2° off substrate).

The observed emission lifetime is

$$\tau = \left(\frac{1}{\tau_r} + \frac{1}{\tau_{nr}} \right)^{-1}, \qquad (6)$$

where τ_r is the average radiative lifetime of free and localised excitons and

$$\tau_{nr} = \tau_{nr}^o e^{E_A/kT} \qquad (7)$$

is an activated nonradiative lifetime.[38] The emission lifetime τ should thus increase with temperature until $\tau_r \approx \tau_{nr}$ and then decrease.[22,37] On the other hand, excitons strongly localized in QD's cannot be characterized by a wave vector and their lifetime should decrease monotonically as the temperature is increased. As can be seen in Fig. 9, a significant increase of the integrated emission lifetime is observed in both samples S4 and S7. This im-
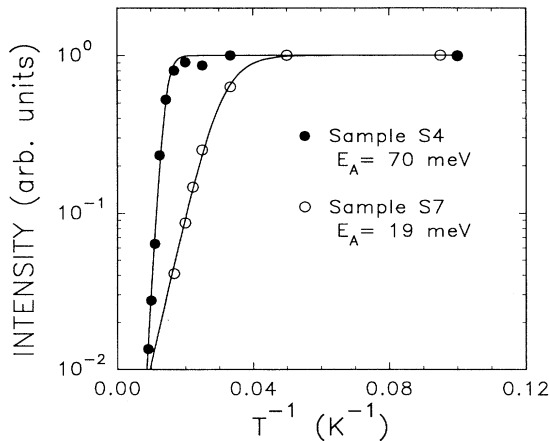
FIG. 10. Arrhenius plot of the time integrated PL intensity for samples S4 [1 ML, (001) oriented subtrate] and S7 (0.3 ML, 2° off substrate). The solid lines show the fits obtained with Eq. (8).

TABLE III. Parameters obtained from a fit using Eq. (8) of the PL integrated intensity as a function of temperature.

Sample	E_A (meV)	τ_r/τ_{nr}^o
S4	70 ± 2	$(1.0 \pm 0.3) \times 10^5$
S7	19 ± 2	$(8.1 \pm 1.5) \times 10^2$

plies that the exciton wave function remains coherent on at least several dots and thus that the InAs nanoclusters form a quantum dot superlattice.

The fact that the peak value of τ is reached at a lower temperature in sample S7 than in sample S4 can be explained by a lower activation energy E_A for the nonradiative process in sample S7. An estimate of E_A for both samples can be obtained by a measurement of the integrated emission intensity, which should vary as a function of temperature as[37]

$$I(T) = I_0 \frac{\tau(T)}{\tau_r(T)} = \frac{I_0}{1 + [\tau_r(T)/\tau_{nr}^o] \exp\{-E_A/kT\}}. \qquad (8)$$

In a first approximation, the temperature dependence of τ_r can be neglected with respect to the strong temperature dependence of the exponential term. Figure 10 shows the integrated emission intensity as a function of temperature for samples S4 and S7, together with fits using Eq. (8). The best values obtained for E_A and τ_r/τ_{nr}^0 are given in Table III. Subtracting the activation energies E_A from the InP band gap, we obtain energy positions which correspond within uncertainty to the peak of the PL emission in the case of sample S4 and which lie in the high-energy part of the PL of sample S7. We thus conclude that the nonradiative process involed corresponds to exciton scattering from the high-energy tail of their distribution in the quantum well or coupled dot systems into the InP barrier states. The fits also yield a scattering time τ_{nr}^o in the range 30–50 fs in the case of sample S4 ($\delta_N = 1$ ML). Similar values were found in other QW systems.[39] On the other hand, τ_{nr}^o is in the ps range in the case of sample S7 ($\delta_N = 0.3$ ML). We interpret this much longer scattering time in terms of a smaller overlap between the InP barrier states and the QD states which results from the more localized character of the excitons in the latter.

VI. CONCLUSIONS

In summary, we have carried out a detailed optical and structural characterization of strained InAs ultrathin quantum wells and nanoclusters grown in an InP matrix by low-pressure metalorganic-vapor-phase epitaxy.

The photoluminescence spectra and the high-resolution x-ray diffraction patterns of the InAs quantum wells show that the InAs layers are coherent with the InP substrate, that the InAs/InP interfaces are sharp, and thus that there is no significant As diffusion in the InP matrix under our growth conditions. The energy positions of the photoluminescence peaks can be well reproduced for cov-

erages of two monolayers and more by a finite square-well model, assuming a valence-band offset of 240 meV. The position of the heavy- and light-hole transitions observed by photoluminescence excitation spectroscopy in a one monolayer quantum well are also in agreement with the predictions of the square-well model.

High-resolution x-ray diffraction measurements performed on samples where fractional monolayers of InAs were deposited on vicinal (001) InP surfaces reveal that InAs nucleates at the terrace boundaries into nanoclusters. Steady-state photoluminescence and photoluminescence excitation spectra show that the InAs nanoclusters laterally confine the excitonic wave function. Time-resolved photoluminescence measurements reveal that interactions between excitons quantum confined in the nanoclusters and phonons or electronic states in the InP matrix are reduced as compared to the one monolayer

InAs quantum well case. Finally, our experiments indicate that there is enough overlap between the excitonic wave function of adjacent nanoclusters to give rise to the formation of delocalized excitonic states. We thus conclude that the InAs nanoclusters form a quantum dot superlattice.

[1] J. M. Gerard and J. Y. Marzin, Appl. Phys. Lett. **53**, 568 (1988).

[2] M. Sato and Y. Horikoshi, J. Appl. Phys. **66**, 851 (1989).

[3] O. Brandt, L. Tapfer, R. Cingolani, K. Ploog, M. Hohenstein, and F. Philipp, Phys. Rev. B **41**, 12599 (1990).

[4] H. Banvillet, E. Gil, R. Cadoret, P. Disseix, K. Ferdjani, A. M. Vasson, A. Tabata, T. Benyattou, and G. Guillot, J. Appl. Phys. **70**, 1638 (1991).

[5] R. P. Schneider, Jr. and B. W. Wessels, J. Appl. Phys. **70**, 405 (1991).

[6] J. F. Carlin, R. Houdré, A. Rudra, and M. Ilegems, Appl. Phys. Lett. **59**, 3018 (1991).

[7] N. Kobayashi and Y. Kobayashi, J. Cryst. Growth **124**, 525 (1992).

[8] C. A. Tran, R. A. Masut, J. L. Brebner, R. Leonelli, J. T. Graham, and P. Cova, J. Cryst. Growth **124**, 596 (1992).

[9] E. Yablanovitch and E. O. Kane, IEEE J. Lightwave Technol. **LT-6**, 1292 (1989).

[10] J. H. Lee, K. Y. Hsieh, and R. M. Kolbas, Phys. Rev. B **41**, 7678 (1990).

[11] P. M. Petroff, A. C. Gossard, and W. Wiegman, Appl. Phys. Lett. **45**, 620 (1984).

[12] K. Asai, J. Cryst. Growth **80**, 425 (1987).

[13] M. Kasu, H. Saito, and T. Kukui, J. Cryst. Growth **115**, 406 (1991).

[14] O. Brandt, L. Tapfer, K. Ploog, R. Bierwolf, M. Hohenstein, F. Phillipp, H. Lage, and A. Heberle, Phys. Rev. B **44**, 8043 (1991).

[15] R. Leonelli, C. A. Tran, R. Tabti, J. L. Brebner, and R. A. Masut, in *Proceedings of the 21st International Conference on the Physics of Semiconductors*, edited by Ping Jiang and Hou-Zhi Zheng (World Scientific, Singapore, 1992), p. 1355.

[16] R. Cingolani, O. Brandt, L. Tapfer, G. Scamarcio, G. C. La Rocca, and K. Ploog, Phys. Rev. B **42**, 3209 (1990).

[17] P. Cova, R. A. Masut, J. Currie, A. Bensaada, R. Leonelli, and C. A. Tran, Can. J. Phys. **69**, 412 (1991).

[18] C. A. Tran, R. A. Masut, P. Cova, and J. L. Brebner, Appl. Phys. Lett. **60**, 589 (1992).

[19] L. Tapfer, M. Ospelt, and H. von Kanel, J. Appl. Phys. **67**, 1298 (1990).

[20] C. R. Wie, J. C. Chen, H. M. Kim, P. L. Liu, Y.-W. Choi, and D. M. Hwang, Appl. Phys. Lett. **55**, 1774 (1989).

[21] P. F. Fewster, Philips J. Res. **41**, 268 (1986).

[22] G. Bacher, J. Kovac, K. Streubel, H. Schweiser, and F. Scholz, Phys. Rev. B **45**, 9136 (1992).

[23] D. Bimberg, J. Christen, T. Fukunaga, H. Nakashima, D. E. Mars, and J. N. Miller, J. Vac. Sci. Technol. B **5**, 1191 (1987).

[24] M. Kohl, D. Heitmann, S. Tarucha, K. Leo, and K. Ploog, Phys. Rev. B **39**, 7736 (1989).

[25] R. F. Schnabel, R. Zimmermann, D. Bimberg, H. Nickel, R. Lösch, and W. Schlapp, Phys. Rev. B **46**, 9873 (1992).

[26] J. Y. Marzin, in *Heterojunctions and Semiconductor Superlattices*, edited by G. Bastard, N. Boccara, M. Lannoo, and M. Voos (Springer-Verlag, Berlin, 1986), p. 161.

[27] *Numerical Data and Functional Relationships in Science and Technology*, edited by O. Madelung, M. Schulz, and H. Weiss, Landolt-Börnstein, New Series III/17a (Springer-Verlag, Berlin, 1982).

[28] J. D. Wiley, in *Semiconductors and Semimetals*, edited by R. K. Willardson and A. C. Beers (Academic Press, New York, 1975), Vol. 10, p. 91.

[29] S. Adachi, J. Appl. Phys. **53**, 8775 (1982).

[30] *Nanostructures and Mesoscopic Systems*, edited by W. P. Kirk and M. A. Reed (Academic Press, New York, 1992).

[31] K. Kash, B. P. Van der Gaag, D. D. Mahoney, A. S. Godz, L. T. Florez, J. P. Harbison, and M. D. Sturge, Phys. Rev. Lett. **67**, 1326 (1991).

[32] T. C. Damen, J. Shah, D. Y. Oberli, D. S. Chemla, J. E. Cunningham, and J. M. Kuo, Phys. Rev. B **42**, 7434 (1990).

[33] J. Aaviksoo, J. Lumin. **48&49**, 57 (1991).

[34] B. Deveaud, T. C. Damen, F. Shah, and C. W. Tu, Appl. Phys. Lett. **51**, 828 (1987).

[35] U. Bockelmann and D. Bastard, Phys. Rev. B **42**, 8947 (1990).

[36] K. Fujiwara, H. Katahama, K. Kanamoto, R. Cingolani, and K. Ploog, Phys. Rev. B **43**, 13978 (1991).

[37] J. Feldman, G. Peter, E. O. Göbel, P. Dawson, K. Moore, C. Foxon, and R. J. Elliott, Phys. Rev. Lett. **59**, 2337 (1987).

[38] M. Gurioli, A. Vinattieri, M. Colocci, C. Deparis, J. Massies, G. Neu, A. Bosacchi, and S. Franchi, Phys. Rev. B **44**, 3115 (1991).

[39] G. Bacher, H. Schweizer, J. Kovac, A. Forchel, H. Nickel, W. Schlapp, and R. Lösch, Phys. Rev. B **43**, 9312 (1990).